

# Magnetohydrodynamical alpha-quenching

Paul Charbonneau and Caroline Dubé

February 26th, 2014

## ABSTRACT

We investigate the physical mechanisms leading to the suppression of the turbulent electromotive force in a EULAG-MHD global magnetohydrodynamical simulation of solar convection producing a large-scale, axisymmetric magnetic component undergoing regular polarity reversals. Assuming the turbulent electromotive force to be linearly related to the large-scale magnetic field, we extract from the simulation the components of the  $\alpha$ -tensor describing this relationship. By segmenting the simulation into temporal blocks and focusing on the high latitudes regions, where a strong dipole component builds up in the simulation, we show that significant suppression of the  $\alpha$ -effect takes place in the course of the large-scale magnetic cycle. The  $\phi\phi$  component of the  $\alpha$ -tensor, the primary contributor to the regeneration of the large-scale poloidal component, can be well reconstructed from the kinetic and magnetic helicities associated with the small-scale flow and field, with a good match in amplitude resulting from assuming a turbulence coherence time smaller than the convective turnover time by a factor of five. Adopting this physical model for the  $\alpha$ -tensor, we go on to show that quenching takes place not only via the growth of the magnetic helicity term, but also through a significant reduction of the kinetic helicity. Nonetheless, our results are generally consistent with the strong quenching paradigm, whereby the  $\alpha$ -effect is suppressed by the small-scale, turbulent magnetic field long before it reaches equipartition with the large-scale magnetic component.

## 1. The solar magnetic cycle and its fluctuations

{sec:intro

The sun's magnetic activity cycle modulates all of solar activity, from radiative variability to the frequency of all geoeffective eruptive phenomena. A proper understanding of the physical mechanism(s) underlying solar dynamo action and regulating the cycle's amplitude and duration are thus a crucial component of space weather, and research on solar-terrestrial interaction in general (Weiss 2010). We are still a long way from physically-based prediction of solar cycle characteristics, even though significant progress has been made in recent

years (for a recent review see Petrovay 2010). Part of the problem lies with the fact that no consensus currently exists as to the mode of operation of the solar cycle; the shearing of the solar magnetic field by differential rotation is near-unanimously considered as a key process, but what drives the regeneration of the solar dipole moment remains ill-understood. Some dynamo models invoke the electromotive force associated with turbulent convection, others the surface decay of active regions (the Babcock-Leighton mechanism), while others yet focus on various rotationally-influenced (magneto)hydrodynamical instabilities taking place immediately beneath the base of the solar convection zone. A survey of these different types of dynamo models can be found in Charbonneau (2010). Most such models make use of geometrical and dynamical simplifications, most notably perhaps the use of the so-called kinematic approximation, in which the magnetic backreaction of the magnetic field on the inductive flows is neglected or parametrized through largely ad hoc prescriptions. Proper tuning of these ad hoc functionals and associated model parameters can in many cases lead to cyclic behavior showing reasonably solar-like variability patterns in the amplitude and duration of magnetic cycles (see, e.g., Karak & Choudhuri 2011; Kitchatinov & Olemskoy 2012; and references therein)

An alternate approach is made possible by global magnetohydrodynamical simulations of solar convection, which recently have succeeded in producing magnetic fields well-organized on large spatial scales and undergoing more or less regular polarity reversals (Augustson et al. 2013; Beaudoin et al. 2013; Brown et al. 2010, 2011; Ghizaru et al. 2010; Käpylä et al. 2010, 2012; Racine et al. 2011). There are no active regions in such simulations (but do see Nelson et al. 2012, 2013), and therefore no Babcock-Leighton mechanism, but the turbulent electromotive force associated with thermally-driven convection is captured in a dynamically consistent manner at spatial and temporal scales resolved by the computational grid. Moreover, magnetic cycles in these simulations undergo significant modulation of their amplitude and period, presumably reflecting the unavoidable stochastic forcing characterizing the turbulent environment in which the large-scale dynamo is operating.

The aim of the present paper is thus to examine in some detail the existence, form and mechanism of suppression for the turbulent electromotive force measured in one such simulation. We first briefly review in §2 the mathematical formalism of mean-field electrodynamics, and attendant definition of the turbulent electromotive force and  $\alpha$ -effect. In section 3 we provide a brief overview of the global magnetohydrodynamical (MHD) numerical simulations providing data for the foregoing analysis, describe the methods used to extract the  $\alpha$ -tensor from this numerical simulation, and compare the result to reconstructions of the  $\alpha$ -tensor based on kinetic and current helicities. The magnetic suppression of the  $\alpha$ -effect taking place in the simulation is investigated in §4, where we also compare our results to  $\alpha$ -quenching parametrizations typically used in mean-field or mean-field-like dynamo models. We close

in §5 by summarizing our conclusions and discussing the limitations of our analyses.

## 2. Mean-field electrodynamics and the $\alpha$ -effect

{sec:mfe}

The mathematical and physical underpinnings of mean-field electrodynamics are well-covered in a number of textbooks and review articles, (Moffat 1978; Krause & Rädler 1980; Ossendrijver 2003; Charbonneau 2013), and consequently only aspects most relevant to the  $\alpha$ -effect and attendant  $\alpha$ -quenching are covered in this section. Mean-field electrodynamics is based on the assumption of scale-separation, according to which the total flow  $\mathbf{U}$  and magnetic field  $\mathbf{B}$  can be separated in large-scale, slowly varying “mean” components  $\langle \mathbf{U} \rangle$  and  $\langle \mathbf{B} \rangle$ , and small-scale, rapidly varying “turbulent” components  $\mathbf{u}'$  and  $\mathbf{b}'$ :

$$\mathbf{B} = \langle \mathbf{B} \rangle + \mathbf{b}' , \quad \mathbf{U} = \langle \mathbf{U} \rangle + \mathbf{u}' , \quad (1) \quad \{\text{eq:scales}\}$$

where the angular brackets represent an averaging operator defined over an intermediate averaging scale such that  $\langle \mathbf{u}' \rangle = 0$  and  $\langle \mathbf{b}' \rangle = 0$ . No restrictions are imposed on the relative magnitudes of large- and small-scale components, but a good separation of scale must exist between  $\mathbf{u}'$ ,  $\mathbf{b}'$  and  $\langle \mathbf{U} \rangle$ ,  $\langle \mathbf{B} \rangle$  for the approach to be physically meaningful. Substituting eq. (1) in the MHD induction equation and applying the averaging operator then leads to an evolution equation for  $\langle \mathbf{B} \rangle$  known as the mean-field induction equation:

$$\frac{\partial \langle \mathbf{B} \rangle}{\partial t} = \nabla \times (\langle \mathbf{U} \rangle \times \langle \mathbf{B} \rangle + \boldsymbol{\mathcal{E}} - \eta \nabla \times \langle \mathbf{B} \rangle) , \quad (2) \quad \{\text{eq:mfhd}\}$$

where

$$\boldsymbol{\mathcal{E}} = \langle \mathbf{u}' \times \mathbf{b}' \rangle \quad (3) \quad \{\text{eq:emf}\}$$

is the (mean) turbulent electromotive force, which acts as a source term. This quantity is then expanded in terms of the mean magnetic field:

$$\mathcal{E}_i = \alpha_{ij} \langle B \rangle_j + \beta_{ijk} \frac{\partial \langle B \rangle_j}{\partial x_k} + \dots , \quad (4) \quad \{\text{eq:alphabet}\}$$

which achieves closure, in the sense that the RHS of eq. (2) no longer depends explicitly on small-scale quantities. For homogeneous, isotropic turbulence,  $\alpha_{ij} = \alpha \delta_{ij}$  and  $\beta_{ijk} = \beta \epsilon_{ijk}$ , so that truncating eq. (4) after the second term and substituting in eq. (2) yields:

$$\frac{\partial \langle \mathbf{B} \rangle}{\partial t} = \nabla \times (\langle \mathbf{U} \rangle \times \langle \mathbf{B} \rangle + \alpha \langle \mathbf{B} \rangle - (\eta + \beta) \nabla \times \langle \mathbf{B} \rangle) . \quad (5) \quad \{\text{eq:mfhd2}\}$$

The  $\alpha$ -term now emerges as a mean-field-aligned electromotive force, and the  $\beta$ -term as turbulent diffusion of the mean magnetic field. Three distinct physical regimes lead to the

same closed-form expression for  $\alpha$  and  $\beta$ : strong magnetic dissipation, weak small-scale magnetic field, or short coherence time for the turbulent flow (leading to the Second Order Correlation Approximation, hereafter SOCA; see, e.g. Ossendrijver 2003; Rempel 2006); all three cases imply that the mean magnetic field suffers little deformation by the small-scale flow, in which case it can be shown that

$$\alpha = -\frac{\tau_c}{3} \langle \mathbf{u}' \cdot \nabla \times \mathbf{u}' \rangle, \quad (6) \quad \{\text{eq:alpha}\}$$

$$\beta = \frac{\tau_c}{3} \langle (\mathbf{u}')^2 \rangle, \quad (7) \quad \{\text{eq:beta}\}$$

with  $\tau_c$  being the coherence time of the turbulent flow. Equation (6) indicates that the isotropic part of the  $\alpha$ -effect is proportional to kinetic helicity  $h_v = \mathbf{u}' \cdot \boldsymbol{\omega}'$ , where  $\boldsymbol{\omega}' = \nabla \times \mathbf{u}'$  is the vorticity associated with the small-scale flow. The kinetic helicity will thus be nonzero in turbulent flows breaking reflection symmetry. In the solar/stellar context, this break is achieved through the agency of the Coriolis force, which imparts cyclonicity on convective updrafts and downdrafts (Parker 1955). In the presence of rotation and stratification, eq. (6) becomes

$$\alpha = -\frac{\tau_c^2}{3} (u'_{\text{rms}})^2 \boldsymbol{\Omega} \cdot \nabla (\rho u'_{\text{rms}}), \quad (8) \quad \{\text{eq:alpha2}\}$$

where  $u'_{\text{rms}} = \sqrt{\mathbf{u}' \cdot \mathbf{u}'}$  (see Steenbeck & Krause 1969). This indicates that the  $\alpha$ -effect is positive (negative) in the Northern (Southern) hemisphere, decreases with decreasing latitudes, and may undergo a sign change at the base of the convection zone due to the rapid drop of the turbulent flow speed when moving down into the stably stratified solar radiative core.

In the magnetohydrodynamical regime, one expects the turbulent electromotive force to be affected by the magnetic field. The pioneering simulations of Pouquet et al. (1976) suggest that for MHD turbulence with short coherence time, eq. (6) should be replaced

$$\alpha = -\frac{\tau_c}{3} (\langle \mathbf{u}' \cdot \nabla \times \mathbf{u}' \rangle - \rho^{-1} \langle \mathbf{j}' \cdot \mathbf{b}' \rangle). \quad (9) \quad \{\text{eq:n1alpha}\}$$

The first term in parentheses on the RHS of this expression is again the kinetic helicity  $h_v$ , and the second is its magnetic equivalent, namely the current helicity, where  $\mu_0 \mathbf{j}' = \nabla \times \mathbf{b}'$ . Note that this magnetic contribution to the  $\alpha$ -effect has a signed opposite to that of the kinetic contribution. This expresses the fact that the small-scale magnetic field induced by the small-scale flow will tend to oppose that flow, a general property of flow-field interactions in the MHD limit.

### 3. Measuring the $\alpha$ -effect

{sec:alpha}

Conceptually, the  $\alpha$ -effect is a kinematic property of the flow, and can be “measured” in a number of ways. The most straightforward is perhaps to impose a uniform large-scale magnetic field across a convecting fluid layer (see, e.g., Brandenburg et al. 1990; Ossendrijver et al. 2001, 2002; Ziegler & Rüdiger 2003; Cattaneo & Hughes 2006; and references therein). The inductive action of the turbulent flow acting on this imposed large-scale magnetic field generates a small-scale magnetic component  $\mathbf{b}'$ , which can be used to compute  $\mathcal{E}$  via eq. (3). The  $\alpha$ -tensor components are then computed by projecting this emf onto the large-scale uniform field. In the context of this *imposed field* approach, it is essential to ensure that (1) the underlying convective flow remains unaffected by the induced magnetic field, so that the  $\alpha$ -effect being measured is really that associated with the original flow, and (2) the turbulent flow itself does not act as a dynamo, in which case the turbulent electromotive force measured in the simulation no longer bears any relation to the imposed mean-field. The *test-field method* (Schrinner et al. 2007), bypasses in principle both of these difficulties by solving a kinematic evolution equation for the small-scale magnetic component, using the flow field from an unmagnetized simulation and a set of weak test magnetic fields (see, e.g., Käpylä et al. 2009). Even then the procedure is delicate as it must often involve periodic resetting of the magnetic field, long temporal averages, can be sensitive to numerical details (cf., e.g., Hughes & Cattaneo 2008).

A more direct approach becomes possible in MHD convection simulations generating autonomously their large-scale magnetic fields. After calculating the mean flow  $\langle \mathbf{U} \rangle$  and magnetic field  $\langle \mathbf{B} \rangle$  through a suitable averaging procedure, eqs. (1) are used to compute the small-scale components  $\mathbf{u}'$  and  $\mathbf{b}'$  by simply subtracting these averages from the total flow  $\mathbf{U}$  and field  $\mathbf{B}$  produced by the simulation. Equation (3) is then used to compute the turbulent electromotive force. In this case the  $\alpha$ -effect being measured is no longer a kinematic property of the unmagnetized flow, but rather the linear relationship characterizing the dependence of  $\mathcal{E}$  on  $\langle \mathbf{B} \rangle$  in the nonlinearly saturated state of the simulation. This “direct” approach was used in Racine et al. (2011), working off a EULAG-MHD convection simulation producing a cycling large-scale axisymmetric magnetic component (see also Ghizaru et al. 2010; Beaudoin et al. 2013; Charbonneau & Smolarkiewicz 2013; Smolarkiewicz & Charbonneau 2013). Zonal averaging then becomes the natural averaging operator, and the  $\alpha$ -tensor components are then extracted from fitting the time series of  $\xi$  and  $\langle \mathbf{B} \rangle$  at each grid point  $(r, \theta)$  in a meridional plane:

$$\langle \xi_j \rangle(r, \theta, t) = \alpha_{jk}(r, \theta) \langle B_k \rangle(r, \theta, t) , \quad j, k = r, \theta, \phi . \quad (10)$$

We follow here Racine et al. (2011) in carrying out a least-squares minimization using Singular Value Decomposition. We do so on the output of a very long duration EULAG-MHD

simulation (1400 yr) shown on on Fig. 1 herein. As with the simulation originally analyzed by Racine et al. (2011), a large-scale magnetic field builds up in this simulation, peaking at  $\sim 0.5$  T is strength, antisymmetric about the equatorial plane and undergoing regular cyclic polarity reversals well-synchronized across hemispheres, on a  $\simeq 40$  yr cadence. The large-scale toroidal component peaks at mid-latitudes and immediately beneath the base of the convecting fluid layers, with an associated dipole moment sharply peaked at polar latitudes and reversing polarity in phase with the internal toroidal component. As detailed in Passos & Charbonneau (2014), the variations in amplitude and duration of successive cycles in this simulation show a number of solar-like characteristics. The analyses of Racine et al. (2011; see also Simard et al. 2013) indicate that these simulations operate as  $\alpha^2\Omega$  dynamo, in the sense that the turbulent emf and shearing by differential rotation both contribute, with comparable magnitude, to the induction of the large-scale toroidal magnetic component.

As with the similar simulation analyzed originally by Racine et al. (2011), the  $\alpha$ -tensor extracted from the simulation of Fig. 1 is full, with off-diagonal components of significant magnitudes, and overall essentially identical to Fig. 9 in Racine et al. (2011). Figure 2A herein focuses on the  $\alpha_{\phi\phi}$  tensor component, one of the two dominant components here and the crucial one in the regeneration of a mean poloidal magnetic component from the mean toroidal field. It shows many features “predicted” by eq. (8), including hemispheric signs, peaks in polar regions, and a sign change near the base of the convecting layers. It also shows a secondary maximum at low latitudes in each hemisphere, a feature seen before at moderate to high rotation rates (see, e.g., Käpylä et al. 2006). Figure 2B shows the associated standard deviation associated with the SVD fitting procedure, which is significantly smaller than the magnitude of  $\alpha_{\phi\phi}$  everywhere except in equatorial regions where  $\langle \mathbf{B} \rangle$  is very small (viz. Fig. 1A), and below the convecting layers where  $\mathcal{E}$  vanishes, in both cases leading to an ill-defined least-squares fitting problem.

The fit defined by eq. (10) is based on a rather severe truncation of eq. (4), yet Racine et al. (2011) could show that the cyclic behavior of the turbulent emf extracted from the simulation is actually well-captured, with the fitting residual showing a  $1/f$  power spectrum extending over one order of magnitude beyond the primary cycle frequency (see their Fig. 10).

We now focus on the reconstruction of the (diagonal)  $\alpha$ -tensor constructed through eq. (9). The calculation of the mean kinetic and current helicities from the simulation output is straightforward, and the results are shown on Fig. 2D and E. Overall, the kinetic helicity has a magnitude larger than the current helicity by a factor  $\sim 5$ , and thus dominates here the reconstruction of the  $\alpha$ -tensor, except in the subsurface layers and at the mid-latitudes at the the base of the convection zone. The other quantity that needs to be extracted from the simulation output is the coherence time  $\tau_c$ . This is now far from straightforward, as

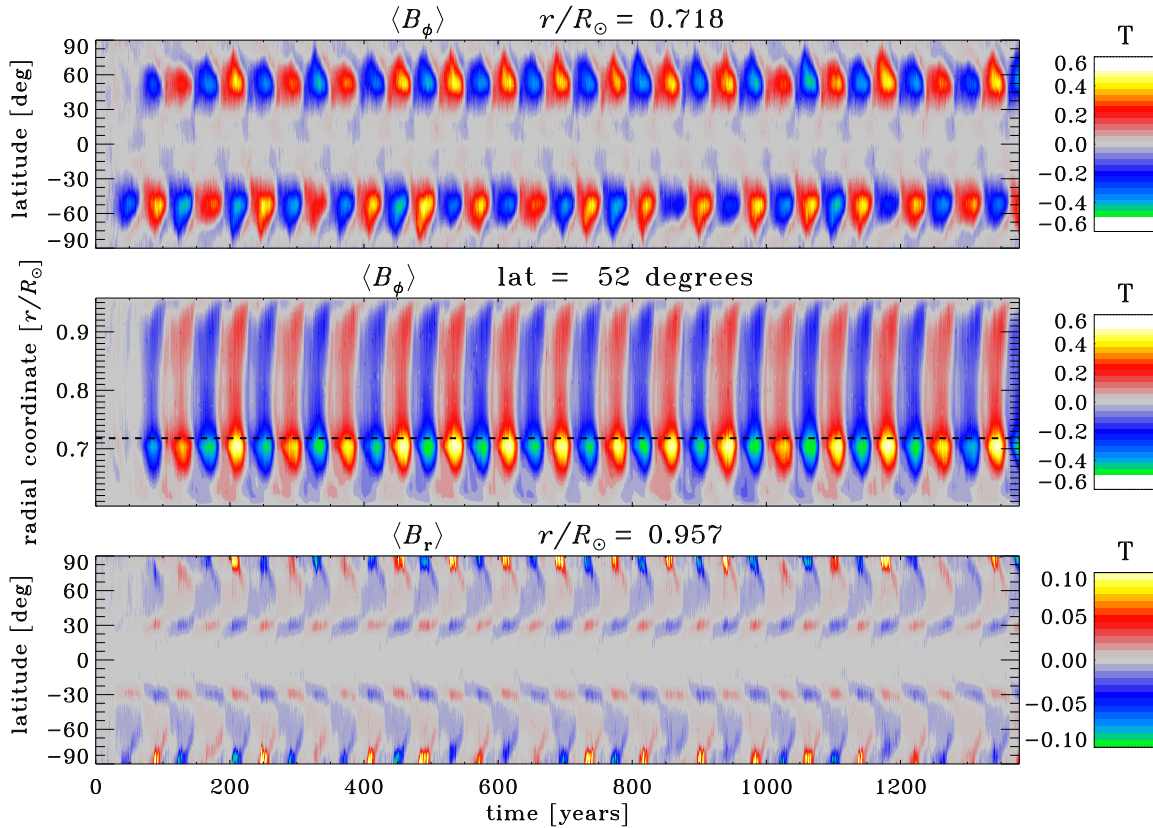


Fig. 1.— Spatiotemporal evolution of the zonally-averaged magnetic field for a long duration EULAG-MHD solar convection simulation. The top panel shows a time-latitude diagram of the zonally-averaged toroidal component at  $r/R = 0.718$ , corresponding to the interface between the convecting fluid layers and the underlying stably stratified fluid layer. Panel (B) shows a time-radius diagram at  $52^\circ$  latitude, where the dashed line indicates the base of the convective zone. The bottom panel shows the zonally-averaged radial magnetic at the outer boundary of the simulation domain ( $r/R = 0.96$ ).

{fig:mhd37a}

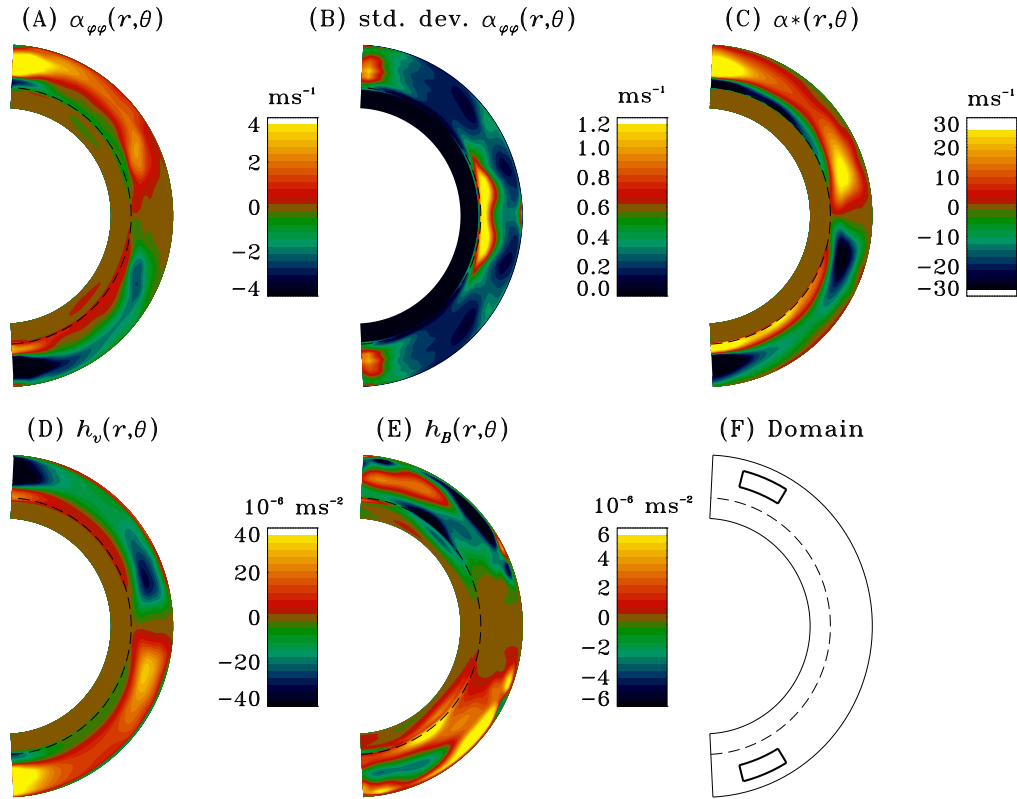


Fig. 2.— The  $\phi\phi$  component of the  $\alpha$ -tensor, as extracted and reconstructed from the simulation. Part (A) shows  $\alpha_{\phi\phi}$  as directly extracted following the SVD-based fitting procedure described in §3, with the associated standard deviation plotted in (B). Part (C) shows  $\alpha^*_{\phi\phi}$  as reconstructed using eq. (9), from the kinetic and magnetic helicity profiles plotted in (D) and (E). Part (F) shows the integration domain used in the  $\alpha$ -quenching analysis of §4.

{fig:alpha}



it involves measuring the lifetime of coherent flow structures developing in the simulation. We follow here Brown et al. (2010) and Racine et al. (2011) in setting this coherence time equal to the eddy turnover time  $\tau_u$ , itself estimated from the rms flow speed and background density scale height:

$$\tau_c = \tau_u = \frac{H_\rho}{u'_{\text{rms}}} . \tag{11} \quad \{\text{eq:tauc}\}$$

This amounts to assuming that the turbulence flow has a Strouhal number  $S \simeq \tau_c/\tau_u$  equal to unity.

Figure 2C shows the tensor diagonal  $\alpha^*$  reconstructed from eq. (9) with  $\tau_c$  estimated in this manner. The resemblance with the actual extracted tensor on part A is striking: both tensor components peak at the poles, show a secondary maximum at low latitudes, and a sign change near the base of the convection zone. Notice, however, the different ranges of the color scales; here  $\alpha^*$  is a factor  $\sim 5$  larger than the actual  $\alpha_{\phi\phi}$  extracted from the simulation. Since the spatial pattern of the tensors are so similar, it becomes natural to assume that the discrepancy arises from an overestimate of the coherence time  $\tau_c$ . Indeed, if one assumes  $\tau_c/\tau_u \simeq 0.2$  instead of unity, so as to recover similar overall amplitudes for  $\alpha^*$  and  $\alpha_{\phi\phi}$ , then a peculiar internal consistency is recovered: we now satisfy one of the conditions under which eqs. (6) and (9) are expected to hold, namely short coherence time turbulence, in the sense that the lifetime of convective eddies is significantly shorter than their turnover time.

#### 4. Measuring $\alpha$ -quenching

{sec:quench}

The turbulent  $\alpha$ -effect is expected to be quenched once the large-scale magnetic field becomes strong enough for magnetic tension to resist deformation by the turbulent flow. However, no consensus exists as to how exactly this takes place, and at which strength of the large-scale field. Many kinematic mean-field dynamo models introduce a simple algebraic amplitude-limiting nonlinearity limiting the growth of the large-scale magnetic field through reduction of the  $\alpha$ -effect. Another approach, known as dynamical  $\alpha$ -quenching, is based on the cascade of magnetic helicity to small-scale. It consists in writing an evolutionary equation for the current helicity  $h_B$ , which is solved simultaneously with the dynamo equation, and with the total  $\alpha$ -effect given by eq. (9) or some closely related form. Recent numerical simulations by Käpylä et al. (2012) even suggest that in the nonlinearly saturated stages of their simulations, the total  $\alpha$ -effect is dominated by its “magnetic” contribution,  $\propto h_B$ .

Since the simulation of Figure 1 produces a large-scale magnetic field and yields a well-defined  $\alpha$ -tensor, it is possible to use the simulation output to investigate whether the latter depends on the former. We first repeat the SVD fitting procedure used to obtain the  $\alpha_{\phi\phi}$

tensor component plotted on Fig. 2A, this time over disjoint 100-month wide temporal blocks centered on epochs of cycle maxima and minima, the latter determined on the basis of the time series of magnetic energy associated with the large-scale magnetic component waxing and waning in the course of the simulation. We opted to integrate the  $\alpha_{\phi\phi}$  component over the domain indicated on Figure 2F. This selected area is one where  $\alpha_{\phi\phi}$  does not change sign, has a magnitude much larger than its variance, and is located at high latitude, where the large-scale dipole moment is building up (viz. Fig. 1C). Henceforth, unless explicitly stated otherwise, averaging is always carried out over this domain, separately for each hemisphere. The results are shown Fig. 3, in the form of bar charts, one bar per temporal block. The error bars assigned to each measurement are obtained by integrating the standard deviation over the same spatial domain as  $\alpha_{\phi\phi}$ , assuming that fluctuations at each grid point are uncorrelated. With only a few exceptions, the  $\alpha_{\phi\phi}$  tensor extracted from each of the 34 cycles in the simulation show a statistically significant difference between epochs of maxima and minima. Qualitatively similar results are obtained for the other components of the  $\alpha$ -tensor.

Next, we carry out a similar exercise, this time extracting the  $\alpha$ -tensor over successive 100-month long temporal block, extending over the whole simulation with a 50% overlap from block to block. For each such block we average the  $\alpha_{\phi\phi}$  component and the magnetic energy over the same spatial domain as before (viz. Fig. 2F). The  $\alpha_{\phi\phi}$  component shows a clear decrease with magnetic energy, dropping from a mean value  $\simeq 4.4 \text{ m s}^{-1}$  at cycle minima, down to  $1.8 \text{ m s}^{-1}$  at cycle maxima, amounting to a reduction by a substantial factor of three. Similar levels of quenching are observed with other  $\alpha$ -tensor components, e.g., the averaged  $\alpha_{r\theta}$  drops from  $1.5$  to  $0.7 \text{ m s}^{-1}$  from cycle minimum to maximum.

We can take advantage of the fact that eq. (9) offers a good representation of the  $\alpha_{\phi\phi}$  component extracted from the simulation (viz. Fig. 2) to investigate the physical origin of the measured  $\alpha$ -quenching. Recall that dynamical  $\alpha$ -quenching assumes that reduction of the  $\alpha$ -effect takes place through the growth of the magnetic term on the RHS of eq. (9). This growth is seen as an unavoidable consequence of magnetic helicity conservation, which requires accumulation of magnetic helicity of one sign at small scales, if a large-scale magnetic component with helicity of opposite sign is to be produced by turbulent dynamo action (Brandenburg 2001). Figure 5 shows the temporal variations of the kinetic helicity  $h_v$  and magnetic helicity  $h_b$  over the course of the 34 cycles in the simulation, in the form of a trajectory in the 2D phase space  $[h_v, h_b]$ . Both helicities are averaged over the high latitude domain depicted on Fig. 2F, as well as in time, over 100-month wide temporal blocks overlapping by 50%, as on Figure 4. The plot shows the trajectory associated with the Northern hemisphere, but the Southern hemisphere trajectory is similar, except for being reflected about the origin. One magnetic cycle corresponds here to one clockwise circuit along the

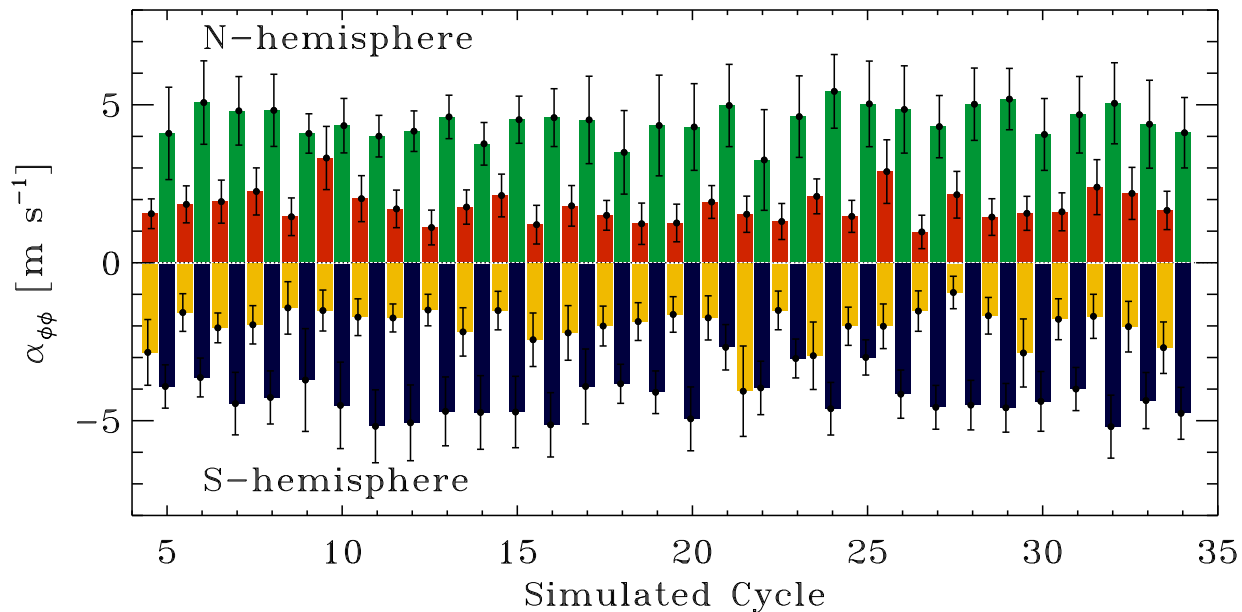


Fig. 3.— Bar diagram showing the magnitude of the  $\alpha_{\phi\phi}$  tensor component, averaged over the domain shown on Fig. 2F. The top (bottom) half of the diagram correspond to the Northern (Southern) hemisphere. The SVD fitting procedure was applied here over 100-month wide segments centered over successive cycle minima (red and yellow) or maxima (green and black). Error bars are estimated by averaging the standard deviation over the same domain, assuming spatially uncorrelated statistics. With only a few exceptions, cycle maxima show a level of  $\alpha$ -quenching significantly exceeding the error bars.

{fig:alpha

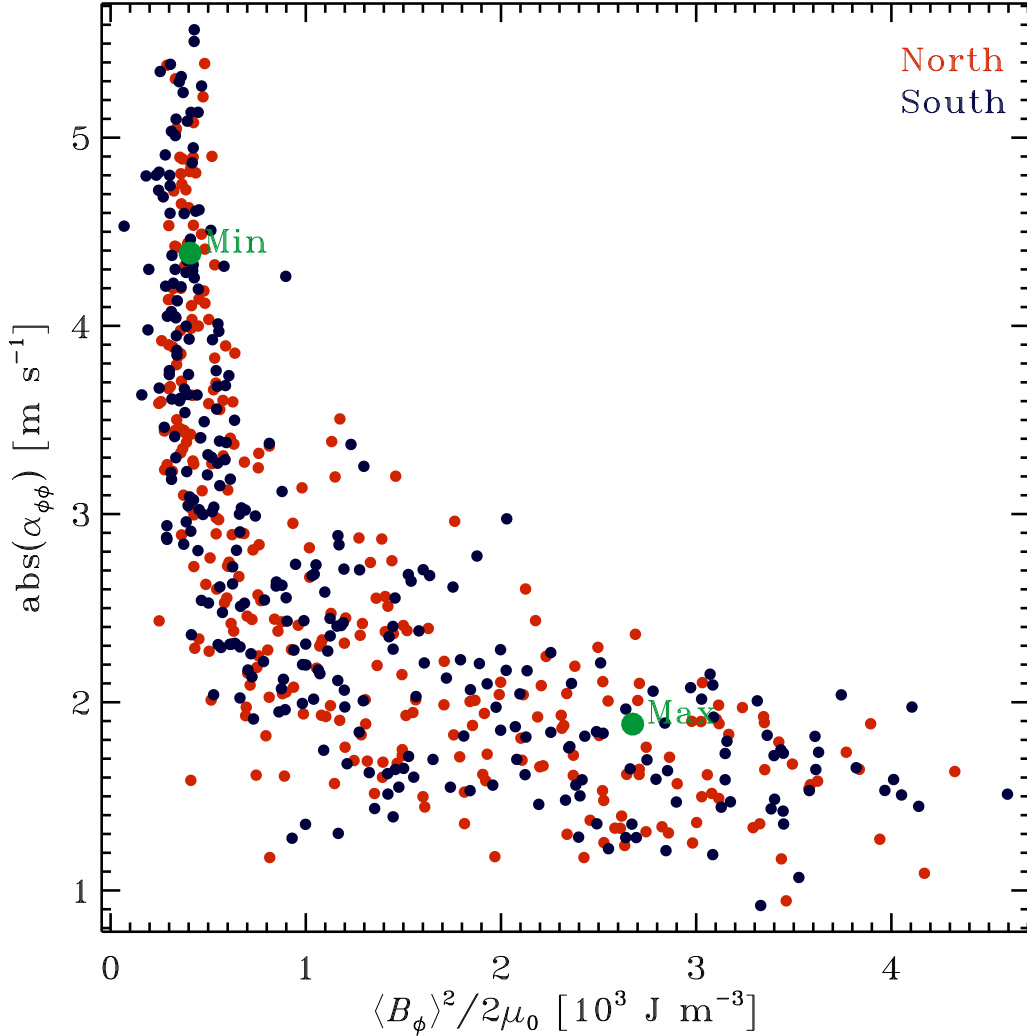


Fig. 4.— Variation of the  $\alpha_{\phi\phi}$  component versus magnetic energy of the zonal magnetic component, both again averaged over the domain shown on Fig. 2F. The SVD fit is carried out over successive 100-month wide time blocks, with 50% overlap between successive blocks, and the magnetic energy is averaged similarly in space and time. The larger green solid dots indicate the mean values for these quantities at cycle maxima and minima, taken directly from Fig. 3.  $\alpha$ -quenching is again quite obvious here, with  $\alpha_{\phi\phi}$  decreasing by a factor of  $\sim 3$  over the range of magnetic energy density sampled throughout the cycles.

{fig:alpha

loop-like path, and the solid green dots show the locii corresponding to the set of maxima and minima on Fig. 3.

The cyclic growth of the current helicity  $h_B$  from cycle minimum to subsequent maximum, followed by a decrease to the next minimum, is generally consistent with the picture of dynamical  $\alpha$ -quenching, according to which the a cascade of magnetic helicity to small-scale during the growth phase of the cycle eventually leads to a saturation of the large-scale dynamo. However, here the kinetic helicity also varies substantially, dropping by almost a factor of two between minima and maxima. In fact, considering the relative magnitudes of  $h_v$  and  $h_b$  (cf. Fig. 2D and E), here this decrease of kinetic helicity contributes twice as much as the growth of current helicity in quenching the  $\alpha$ -effect. Interestingly, in the descending phase of the cycles the decrease of current helicity leads significantly the rebuilding of kinetic helicity, a possible indication that dissipation at small scales is already starting to destroy magnetic helicity even before cycle maximum is reached.

The numerical simulation of Figure 1 achieves stability through implicit diffusivities associated with the numerical advection scheme, which here is the same for the advection of fluid velocity and magnetic field; in other words, here the magnetic Prandtl number is expected to be of order unity. The rather complex variation of kinetic versus current helicity is therefore unexpected, and must originate not with the dissipative properties of the simulation, but rather with changes in the character of the small-scale flows, likely mediated by the large-scale magnetic field and perhaps also time-varying large-scale flows.

Further insight into the quenching mechanism can be obtained by investigating the ways in which the helicities vary in the course of the cycle. Kinetic helicity can decrease either through a general decrease of the rms small-scale flow speed, or through decreasing alignment between  $\mathbf{u}'$  and  $\boldsymbol{\omega}' = \nabla \times \mathbf{u}'$ . Likewise, current helicity can decrease either because the small-scale magnetic field decreases, or becomes increasingly misaligned with the small-scale electrical current density  $\mathbf{j}' = \mu_0^{-1} \nabla \times \mathbf{b}'$ . These quantities can all be extracted from the numerical simulation output, and once again averaged over our now customary integration domain of Fig. 2F. Figure 6 shows phase space trajectories between the alignment angle and flow/field magnitude for kinetic helicity in (A), and current helicity in (B). These alignment angles are defined here through:

$$\cos \theta_v = \frac{h_u}{|\mathbf{u}'| |\boldsymbol{\omega}'|} , \quad \cos \theta_b = \frac{h_b}{|\mathbf{b}'| |\mathbf{j}'|} , \quad (12) \quad \{\text{eq:angles}\}$$

both averaged over the usual integration domain. The plots show the trajectories for the Northern hemisphere; similar trajectories are observed in the Southern hemisphere.

The decrease of kinetic helicity from cycle minimum to maximum is seen to originate in approximately equal part with a decrease of the rms flow speed, and decreasing alignment

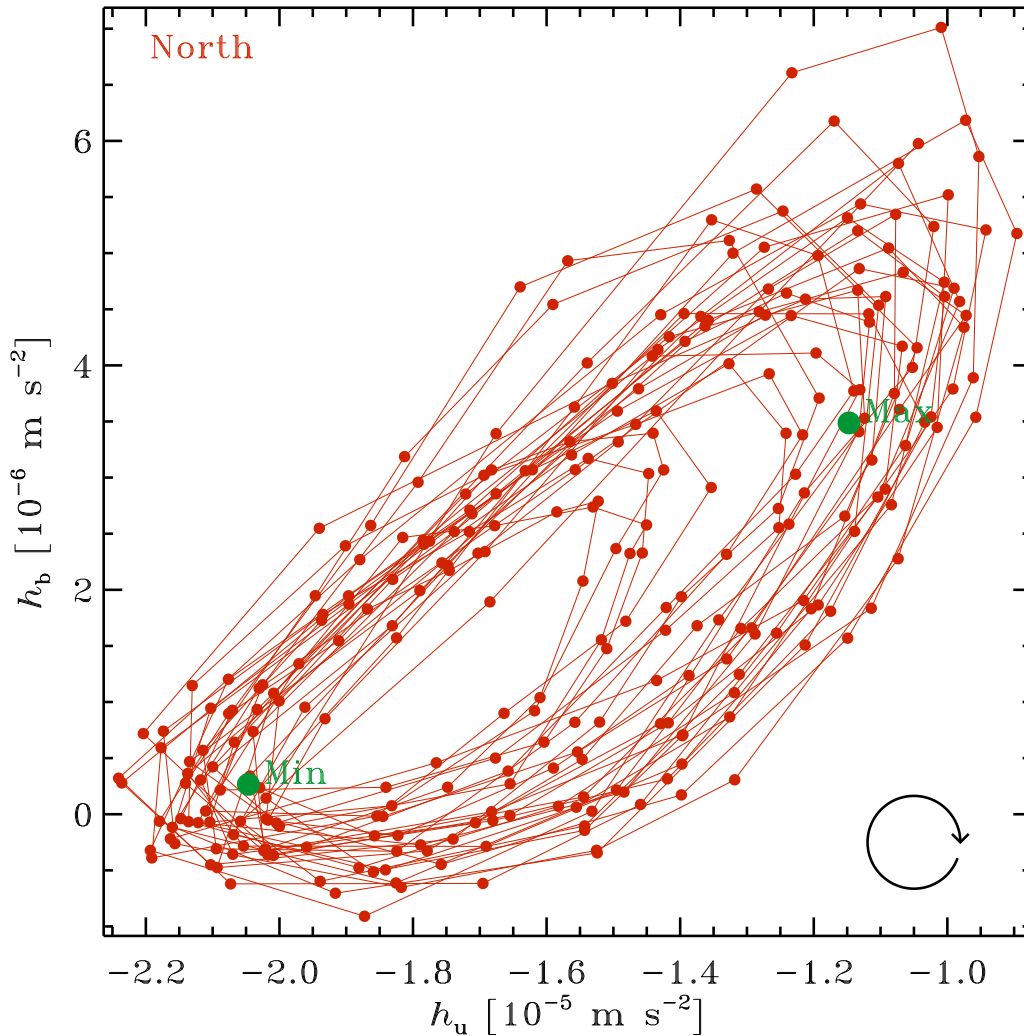


Fig. 5.— Phase space portrait of the joint variations of the kinetic and current helicities in the Northern hemisphere. As in previous Figures,  $h_v$  and  $h_B$  are averaged over the domain shown on Fig. 2F and averaged over successive 100-month wide temporal blocks with 50% overlap (solid dots), with consecutive blocks connected by a line segment. The trajectory runs clockwise on this plot, with mean values over cycle maxima and minima indicated by solid green dots.

{fig:alpha}

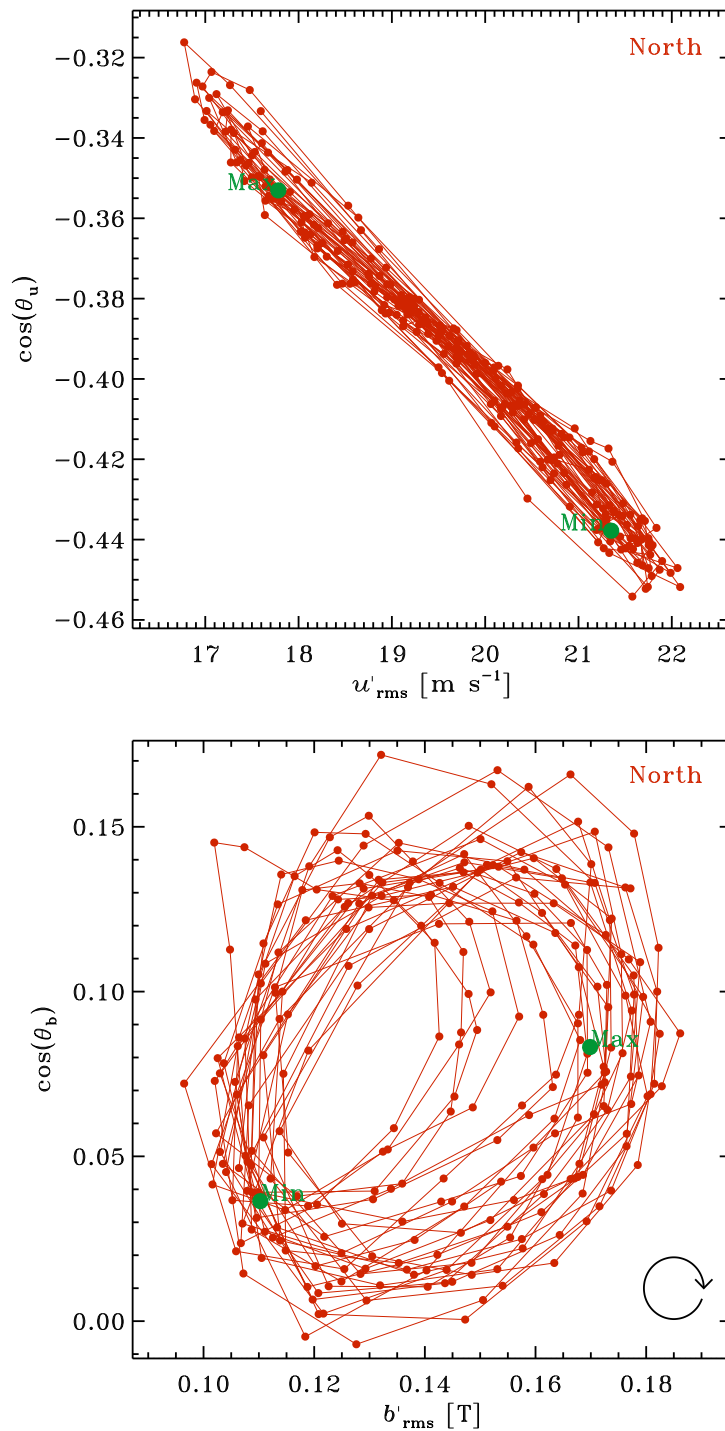


Fig. 6.— Phase space portrait of the cyclic variations of kinetic (top) and current (bottom) helicities in the Northern hemisphere, each panel in a format similar to Fig. 5. The trajectory runs clockwise on the bottom plot, with mean values over cycle maxima and minima again indicated by the larger green dots on each panel. The rms turbulent flow speed varies in phase with the angle it subtends with vorticity, but in the case of current helicity the angle between  $\mathbf{b}'$  and  $\mathbf{j}'$  is out of phase by  $\sim \pi/2$  with the variation of  $b'_{\text{rms}}$  (see text).

{fig:2help}

between the flow and its vorticity, both varying tightly in phase throughout the magnetic cycle. The pattern leading to the variation of current helicity is more complex, however. The small-scale magnetic field  $\mathbf{b}'$  and electrical current density  $\mathbf{j}'$  remains almost orthogonal to one another across the cycle ( $\cos\theta_b \simeq 0$ ), departure from orthogonality peaking in the descending phase and vanishing upon approaching minimum in the descending phase.

The  $\alpha$ -quenching parametric formulae most often used in mean-field dynamo models are based on the assumption that the  $\alpha$ -effect becomes suppressed once turbulent fluid motions reach energy equipartition with the large-scale magnetic field, i.e.,:

$$\frac{1}{2}\rho(u'_{\text{rms}})^2 = \frac{\langle \mathbf{B} \rangle^2}{2\mu_0} \quad (13)$$

This working hypothesis is most often introduced in mean-field models by adding an explicit algebraic dependence on  $\langle \mathbf{B} \rangle$  to the  $\alpha$ -tensor components:

$$\alpha \rightarrow \frac{\alpha}{1 + (\langle \mathbf{B} \rangle^2 / B_{\text{eq}})} \quad (14)$$

This ad hoc expression obviously “does the right thing”, in that it ensures  $\alpha \rightarrow 0$  as  $\langle \mathbf{B} \rangle \gg B_{\text{eq}}$ . However, attempts to validate such expression against MHD numerical simulations of forced helical toy flows have instead lead to the alternate “strong quenching” expression:

$$\alpha \rightarrow \frac{\alpha}{1 + R_m (\langle \mathbf{B} \rangle^2 / B_{\text{eq}})} \quad (15)$$

where  $R_m$  is the magnetic Reynolds number characterizing the flow. With  $R_m \sim 10^8$ – $10^{10}$  in solar convection zone,  $\alpha$ -quenching then sets in at a magnitude of  $\langle \mathbf{B} \rangle$  four to five orders of magnitude below equipartition. The difference between eqs. (14) and (15) hinges on the fact that at high- $R_m$ , the turbulent flow first reaches energy equipartition with  $\mathbf{b}'$ , not  $\langle \mathbf{B} \rangle$ ; eq. (15) then follows from the scaling ratio  $\mathbf{b}' / \langle \mathbf{B} \rangle \sim \sqrt{R_m}$ , expected in the limit  $R_m \gg 1$  (see Cattaneo & Hughes 1996).

In the simulation used in this paper  $\rho = 42 \text{ kg m}^{-3}$  and  $u'_{\text{rms}} \simeq 20 \text{ m s}^{-1}$  in the middle of averaging domain used for the  $\alpha$ -quenching analysis, which leads to a kinetic energy density  $e_k \simeq 8000 \text{ J m}^{-3}$ . This value corresponds to an equipartition field strength of  $\simeq 0.15 \text{ T}$ , in remarkable agreement with the centroid value on Fig. 6. On the other hand, examination of Fig. 4 indicates that quenching is already well underway at  $\langle B_\phi \rangle^2 / 2\mu_0 \simeq 10^3 \text{ J m}^{-3}$ . This suggests that that  $\alpha$ -quenching in our simulation is mediated primarily by small-scale magnetic field, in agreement with the strong quenching Ansatz, even though here  $R_m \simeq 50$ , which, while definitely larger than unity, is still a long way from  $10^8$ . Note that this conclusion relies on the use of the toroidal component of the large-scale magnetic field to compute these energy density, since  $\alpha_{\phi\phi}$  operates on this magnetic component; calculating



the magnetic energy using all large-scale field components leads to a smaller ratio between magnetic energies at large and small scales, a consequence of the strong dipole moment building up in the simulation.

## 5. Concluding remarks

{sec:concl

In this paper we extracted the  $\alpha$ -tensor from a temporally extended EULAG-MHD simulation of solar convection, producing a well-defined large-scale axisymmetric magnetic component undergoing regular cyclic polarity reversals. The specific simulation we use spans 18 magnetic cycles of period  $\simeq 80$  yr, equivalent to 36 “solar activity cycles”. These magnetic cycles are characterized by reasonably stable amplitudes, durations, and show good hemispheric synchrony. Mean-field-based analyses modelling of similar simulations (Racine et al. 2011; Simard et al. 2013) suggest that they operate as  $\alpha^2\Omega$  dynamos, in which the cycle regeneration of the large-scale poloidal magnetic component is mediated by a mean-field-aligned turbulent electromotive force.

To a first approximation the  $\alpha$ -tensor relating the mean magnetic field to the mean turbulent emf is found to be independent of the phase of the cycle, and its  $\phi\phi$  component, crucial to the regeneration of the dipole moment, turns out to be well-represented by classical expressions computed in the context of the SOCA approximation. These expressions (viz. eqs. (6) and (9) herein) relate the isotropic part of the  $\alpha$ -tensor to the mean kinetic and current helicities of the small-scale flow and magnetic field, and are applicable to near-homogeneous, near-isotropic turbulence. We conjecture that the good agreement so obtained results from the low coherence time of the small-scale turbulent flow building up in our simulation, which is one of the physical regimes under which SOCA is expected to hold.

Focusing on the  $\phi\phi$  component of the  $\alpha$ -tensor, we could show that significant magnetic quenching of the  $\alpha$ -effect is taking place at high latitudes, where a strong axisymmetric dipole moment builds up in the simulation. Taking the SOCA expression for  $\alpha_{\phi\phi}$  at their face value, we sought to track the origin of the measured quenching to magnetically-mediated variations in the kinetic and current helicities. Our analysis shows that quenching of the  $\alpha$ -effect takes place not only through a growth of the current helicity, but also by a decrease of the kinetic helicity. Approximately half of this decrease is due to a drop in the rms turbulent flow speed, while the other half results from a change in the alignment of the small-scale flow with respect to its vorticity vector. These results indicate that, at least in this simulation, quenching of the  $\alpha$ -effect is a fully magnetohydrodynamical phenomenon, finding its roots in magnetically-mediated changes in the patterns of turbulent convection.

Independently of the applicability (or lack thereof) of the SOCA expressions for the  $\alpha$ -tensor, our analysis indicates that even in the minimum phase of the magnetic cycles our  $\alpha$ -effect shows a strong dependence on magnetic energy, indicating that significant magnetic quenching is acting already then. Our  $\alpha$ -effect evidently operates in a strongly nonlinear regime at all phases of the large-scale magnetic cycles unfolding in the simulations, as seems to also be the case in the simulations of Käpylä et al. (2012, 2013). We also compared our quenching results to algebraic quenching formulae commonly used as amplitude-limiting nonlinearities in many mean-field and mean-field-like models of solar and stellar dynamos. Our results are consistent with the so-called strong quenching Ansatz, whereby quenching of the  $\alpha$ -effect is effected primarily by the small-scale magnetic field component, rather than directly by the large-scale magnetic component defining the cycles.

In light of these results, it is tempting to conclude that magnetic quenching of the turbulent electromotive force is the mechanism controlling here the amplitude of the large-scale magnetic cycle. However, parallel analyses of similar simulations have shown that the cycle also drives solar-like torsional oscillations of the internal differential rotation (Beaudoin et al. 2013), and modulates the large-scale meridional flow also building up in the simulation (Passos et al. 2012). All these processes represent transfer of magnetic energy to kinetic energy, and thus can also contribute to the saturation of the large-scale magnetic cycle. A detailed energy balance analysis is currently under way to identify which of these mechanism dominates the draining of the magnetic energy reservoir (Passos et al., in prep.). While these simulations are still far removed from solar conditions, the hope remains that the detailed diagnosis and analyses they permit may shed some light on the mechanisms controlling the amplitude and duration of the real solar cycle, and offer a quantitative springboard towards a similar understanding of observed stellar cycles.

This work was supported by a Discovery Grant from the Natural Sciences and Engineering research Council of Canada, the Canadian Foundation for Innovation, and time allocation on the computing infrastructures of Calcul Québec, a member of the Compute Canada consortium.

## REFERENCES

- Augustson, K., Brun, A.S., Miesch, M.S., & Toomre, J. 2014, ApJL, submitted
- Beaudoin, P., Charbonneau, P., Racine, É., & Smolarkiewicz, P.K. 2013, SolP, 282, 335
- Brandenburg, A., Tuominen, I., Nordlund, Å., Pulkkinen, P., Stein, R.F. 1990, A&A, 232, 277

- Brandenburg, A. 2001, *ApJ*, 550, 824
- Brown, B.P., Browning, M.K., Brun, A.S., Miesch, M.S., & Toomre, J. 2010, *ApJ*, 711, 424
- Brown, B.P., Miesch, M.S., Browning, M.K., Brun, A.S., & Toomre, J. 2011, *ApJ*, 731, id69
- Cattaneo, F., & Hughes, D.W. 1996, *PRE*, 54, 4532
- Cattaneo, F., & Hughes, D.W. 2006, *JFM*, 553, 401
- Charbonneau, P. 2010, *LRSP*, 7, 3
- Charbonneau, P. 2013, *Solar and Stellar Dynamos*, 39<sup>th</sup> Saas Fee Advanced Course, Springer
- Charbonneau, P., & Smolarkiewicz, P. K. 2013, *Science*, 340, 42
- Ghizaru, M., Charbonneau, P. & Smolarkiewicz, P. K. 2010, *ApJ*, 715, L133
- Hughes, D.W., & Cattaneo, F. 2008, *JFM*, 594, 445
- Karak, B.B., & Choudhuri, A.R. 2011, *MNRAS*, 410, 1503
- Käpylä, P.J., Korpi, M.J., Tuominen, I. 2006, *AN*, 327, 885
- Käpylä, P.J., Korpi, M.J., Brandenburg, A. 2009, *A&A*, 500, 633
- Käpylä, P.J., Korpi, M.J., Brandenburg, A., Mitra, D., & Tavakol, R. 2010, *AN*, 331, 73
- Käpylä, P.J., Mantere, M.J., Brandenburg, A. 2012, *ApJL*, 755, idL22
- Käpylä, P.J., Mantere, M.J., Cole, E., Warnecke, J., & Brandenburg, A. 2013, *ApJ*, 778, id41
- Kitchatinov, L.L., & Olemskoy, S.V. 2012, *SolP*, 276, 3
- Krause, F., & Rädler, K.-H. 1980, *Mean-field magnetohydrodynamics and dynamo theory*, Oxford: Pergamon Press. 271pp.
- Moffatt, H. K. 1978, *Magnetic Field Generation in Electrically Conducting Fluids* (Cambridge: Cambridge Univ. Press)
- Nelson, N.J., Brown, B.P., Brun, A.S., Miesch, M.S., & Toomre, J. 2013, *ApJ*, 762, id73
- Nelson, N.J., Brown, B.P., Brun, A.S., Miesch, M.S., & Toomre, J. 2014, *SolP*, 289, 441
- Ossendrijver, M.A.J.H., Stix, M., & Brandenburg, A. 2001, *A&A*, 376, 713

- Ossendrijver, M.A.J.H., Stix, M., Brandenburg, A., & Rüdiger, G. 2002, *A&A*, 394, 735
- Ossendrijver, M. 2003, *A&A Rev.*, 11, 287
- Parker, E. N. 1955, *ApJ*, 122, 293
- Passos, D., Charbonneau, P., & Beaudoin, P. 2012, *SolP*, 279, 1
- Passos, D., & Charbonneau, P. 2014, *A&A*, submitted
- Petrovay, K. 2010, *LRSP*, 7, 6
- Pouquet, A., Frisch, U., & Leorat, J. 1976, *JFM*, 77, 321
- Prusa, J. M., Smolarkiewicz, P. K. & Wyszogrodzki, A. A. 2008, *Comp. Fluids*, 37, 1193
- Racine, É., Charbonneau, P., Ghizaru, M., Bouchat, A. & Smolarkiewicz, P. K. 2011, *ApJ*, 735, 46
- Rempel, M. 2006, in *Heliophysics I*, eds. C.J. Schrijver & G.L. Siscoe, Cambridge University Press, 42
- Schrinner, M., Rädler, K.-H., Schmitt, D., Rheinhardt, M., & Christensen, U.R. 2007, *GAFD*, 101, 81
- Simard, C., Charbonneau, P., & Bouchat, A. 2013, *ApJ*, 768, id16
- Smolarkiewicz, P. K. & Charbonneau, P. 2013, *JCP*, 236, 608
- Steenbeck, M., & Krause, F. 1969, *AN*, 291, 49
- Smolarkiewicz, P. K. & Charbonneau, P. 2013, *JCP*, 236, 608
- Weiss, N.O. 2010, *Astr. Geophys.*, 51, 3.09
- Ziegler, U., & Rüdiger, G. 2003, *A&A*, 394, 735